PERGAMON

Journal of Structural Geology 23 (2001) 93–112

JOURNAL OF STRUCTURAL GEOLOGY

www.elsevier.nl/locate/jstrugeo

Calcite and quartz microstructural geothermometry of low-grade metasedimentary rocks, Northern Range, Trinidad

John C. Weber[a,*], David A. Ferrill[b], Mary K. Roden-Tice[c]

[a]*Department of Geology, Grand Valley State University, Allendale, MI 49401, USA*
[b]*Center for Nuclear Waste Regulatory Analyses, Southwest Research Institute, San Antonio, TX 78238, USA*
[c]*Department of Earth and Environmental Sciences, SUNY-Plattsburgh, Plattsburgh, NY 12901, USA*

Received 15 September 1999; accepted 10 May 2000

Abstract

The Northern Range of Trinidad is a mountainous exposure of deformed metasedimentary rocks with Mesozoic depositional ages and Tertiary metamorphic ages located in the Caribbean–South American plate boundary zone. These rocks lack precise mineralogical indicators of metamorphic grade. Using temperature-sensitive quartz and calcite microstructures, and fission track data, we identify, describe, quantify, and map a nearly continuous spectrum of relatively low (>l50°C) to relatively high (250–400°C) deformation temperatures from east to west across the range. Average estimated rock exhumation rates also increase systematically along this trend. The analysis illuminates a sharp, east–west-trending, major thermal discontinuity (i.e. a fault) along the southern boundary of the range. Kinematic analysis of faults and shear bands adjacent to this boundary and modeling indicate that the fault probably dips southward at 80–85° and accommodated normal dip-slip at rates that decreased from west to east. Earlier experimental studies at high strain rates illustrated a strong strain rate dependency for quartz microstructural transitions. Our work indicates a possible strong temperature control for quartz microstructural transitions at natural strain rates.

1. Introduction

The Northern Range of Trinidad is an east–west-trending mountainous exposure of subgreenschist to lower greenschist grade metasedimentary rocks (e.g. Frey et al., 1988) located in the Caribbean–South American plate boundary zone (Fig. 1a, b). Global positioning system data show that the Carribean plate currently moves ~20 mm/year N86°E ± 2° near Trinidad (Weber et al., 2000). Rocks in the Northern Range are predominantly slates, schists, metaquartzites, and metacarbonates. The protoliths from which these rocks were derived are interpreted to have been deposited on a north facing passive margin along northern South America that developed in response to Pangaea breakup, rifting, and drifting (e.g. Pindell, 1985; Speed, 1985). Relict fossils from scattered localities indicate Tithonian to Maastrichtian (−150 to 67 Ma; e.g. Saunders, 1972) protolith depositional ages. $^{40}Ar/^{39}Ar$ spectra from metamorphic white micas indicate subsequent mid-Tertiary metamorphism (Foland et al., 1992a; Foland and Speed, 1992b), which was likely synkinematic with transpression and oblique Caribbean–South American plate convergence (Speed, 1985, 1986; Robertson and Burke, 1989; Russo and Speed, 1992; Algar and Pindell, 1993). These deformed metasedimentary rocks were then exhumed and uplifted during the Neogene forming today's rugged mountains.

The only comprehensive published study of Northern Range metamorphism is that of Frey et al. (1988), which applied mineral paragenesis techniques and demonstrated peak paleotemperatures of 300–400°C, but could resolve no internal variations in grade. Frey et al. (1988) however speculated on a possible east-to-west increase in grade based on changes in rock "field character" (also see reference therein to Craig, 1907). They reasoned that because relict sedimentary fabrics are common in the eastern Northern Range, but not in the central and western parts of the range, grade probably increases toward the west, perhaps abruptly across an inferred Grand Riviere fault (Kugler, 1961; Barr, 1963; Fig. 1b).

Frey et al.'s (1988) inability to resolve grade variations in the sub-greenschist to greenschist grade metasedimentary rocks of the Northern Range illustrates a common and more general problem, the inability to characterize the structural architecture in similar parts of many other orogenic belts. This problem is mainly due to an intrinsic lack of precision from the available metasedimentary geothermorneters (and geobarometers), and limited distributions of

* Corresponding author.
E-mail address: weber@gvsu.edu (J.C. Weber).

0191-8141/01/$ - see front matter
PII: S0191-8141(00)00066-3

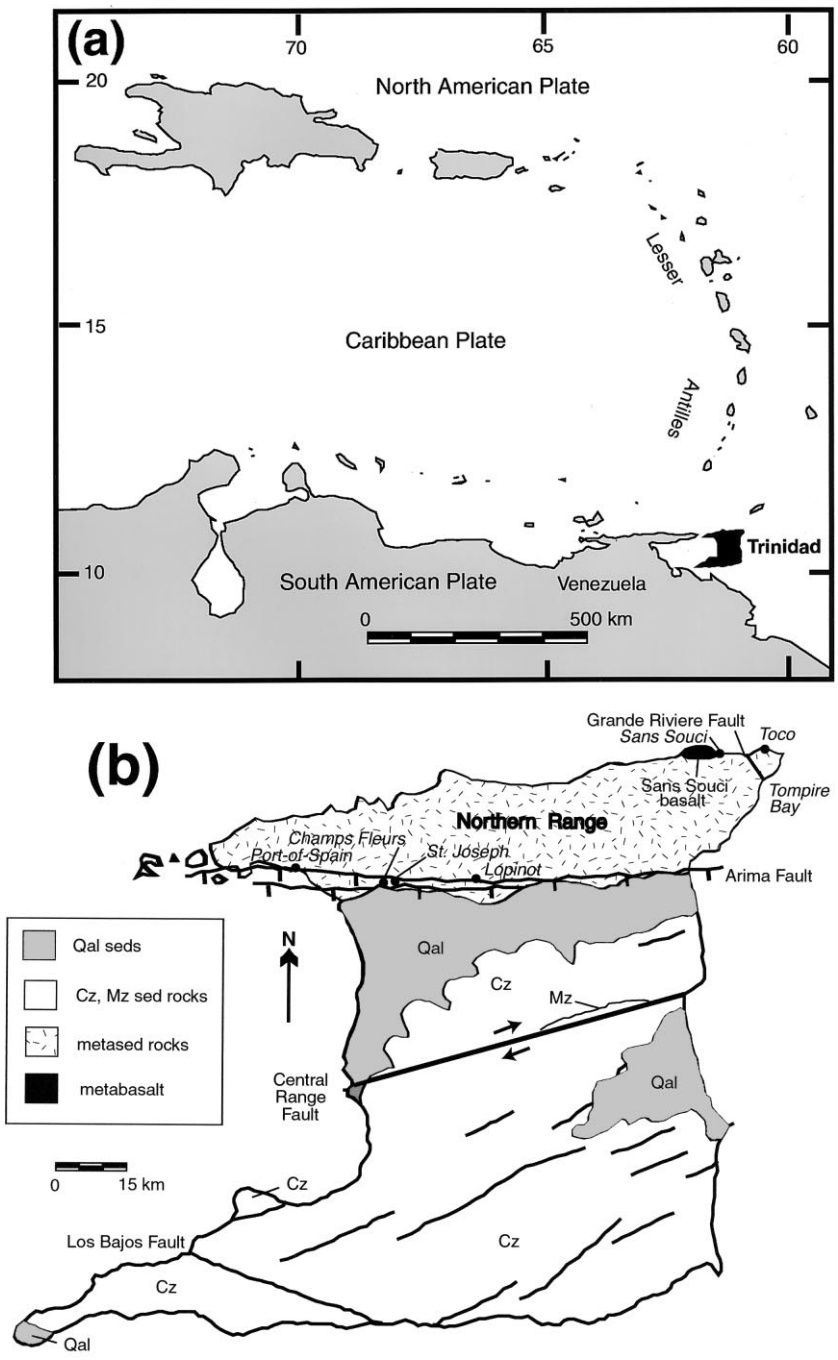

Fig. 1. (a) Map showing the location of the Caribbean, South American, and North American plates, and the island of Trinidad. Atlantic seafloor of the North and South American plates subducts beneath the Caribbean plate east of the Lesser Antilles arc. The plate boundary zones between the Caribbean plate and the North and South American plates contain many individual faults not shown. (b) Geologic and location map of Trinidad. Geology simplified from Kugler (1961). With the exception of the Sans Souci basalt, rocks in the Northern Range are metasedimentary with Mesozoic protolith ages and Cenozoic metamorphic ages. Sediments and sedimentary rocks of Quaternary (Qal), Cenozoic (Cz), and Mesozoic (Mz) ages cover the rest of the island. Fault traces and macrofold axes shown as heavy dark lines. Names are given for some of the major faults; sense of slip not shown where it is not well documented. The fault at the southern boundary of the Northern Range, discussed in the text, is shown schematically and is referred to as the Arima fault after Kugler (1961); tick marks on down-thrown side. The Central Range Fault is currently the active, but aseismic and possibly locked, strike-slip fault in this segment of the plate boundary zone and slips at 14 ± 2 mm/year (Weber et al., 1999, 2000).

age- and lithology-dependent low-grade metamorphic indicators. Precise low-grade mineral paragenesis data are available mainly from metavolcanic, especially meta-basaltic, rocks (Liou et al., 1987; Schmidt and Robinson, 1997). Other low-grade metasedimentary geothermometers include those derived from conodont color alteration (Harris, 1979), vitrinite reflectance (Teichmuller, 1987), and illite crystallinity (Kish, 1987; Frey, 1987). In the

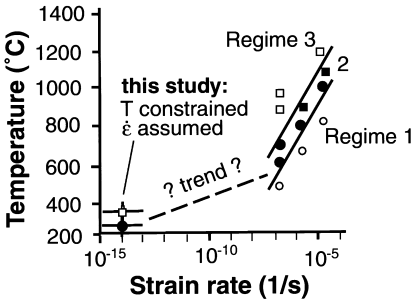

Fig. 2. Quartz microstructural regimes (1–3), defined with respect to experimental temperature (~500–1300°C) and strain rate (10^{-7}–$10^{-4}s^{-1}$) stability fields after Hirth and Tullis (1992, fig. 2a, "As is") and natural conditions (this study). Open circles represent Regime 1, filled circles represent Regime 2, open squares represent Regime 3, and filled squares represent gradations between Regimes 2 and 3. Only temperature is constrained in the present study; the natural strain rates shown are assumed (see text for further discussion).

Frey et al. (1988) Northern Range study, relative grade differences were not resolved using illite crystallinity because of interference of illite X-ray diffraction peaks with those from other sheet silicates. Because the Northern Range protoliths were Mesozoic in age, no conodonts are present in these rocks. Furthermore, the lack of widespread vitrinite and metavolcanic material makes reflectance and mineral paragenesis techniques largely inapplicable.

In this paper, we present a study of temperature-sensitive quartz and calcite microstructures in metaquartzite and metacarbonate rocks from across the Northern Range. We also incorporate independent new and published (Algar, 1993; Algar et al., 1998) apatite and zircon fission track data and metamorphic mineralogical constraints (Frey et al., 1988) into our analysis. We use these data to: (1) estimate lateral variations in deformation temperatures (thermal grade) and rock exhumation rates across the Northern Range, (2) substantiate and better calibrate the temperatures at which key transitions take place between microstructural assemblages in naturally deformed calcite, and (3) calibrate the temperatures at which key transitions take place in microstructural assemblages in naturally deformed quartz.

We identify, describe, and map a possibly continuous, east-to-west spectrum of relatively low (>l50°C) to high (300–400°C) deformation temperatures across the Northern Range, confirming Frey et al.'s (1988) speculation of a westward increase in grade. Our results do not allow us to resolve whether the increase in thermal grade is abrupt across the inferred Grand Riviere fault (Fig. 1b) and permit the interpretation that throw across this fault may be either insignificant or nonexistent. The most significant break in thermal grade occurs along the southern boundary of the range (Fig. 1b). We discuss published interpretations, present new fault kinematic data, and develop and discuss kinematic models regarding the southern boundary fault. Our results substantiate the relatively new (Ferrill, 1991; Burkhard, 1993) calcite microstructural geothermometry technique, provide initial empirical calibration of quartz microstructural geothermometers, and place important new constraints on interpretations of the tectonics of the Caribbean–South American plate boundary zone.

2. Geothermometry methods

2.1. Calcite microstructure geothermometry

One of the principal mechanisms by which calcite takes up crystal plastic strain at low temperatures is mechanical twinning (Ferrill and Groshong, 1993). Combining observations from experiments and naturally deformed rocks with independent temperature constraints has demonstrated that calcite twin morphology is strongly dependent on temperature of deformation (Groshong et al., 1984; Ferrill, 1991; Burkhard, 1993; Ferrill, 1998). Natural deformation of coarse calcite at temperatures below 150–200°C tends to produce thin, Type I twins that have no petrographically observable width of twinned calcite (Ferrill, 1991). Such twins are generally <1 μm wide. Natural deformation at increased temperatures produces straight thick Type III twins at 150–300°C, curved thick twins and irrational (Turner and Orozco, 1976) twins (Type HI microstructures) at >200°C, and thick patchy twins and recrystallized twins (Type IV microstructures) at >250°C (Ferrill, 1991; Burkhard, 1993). Dynamic recrystallization of coarse calcite begins at temperatures above 250°C. Complete dynamic recrystallization, designated as the Type V calcite microstructure in this study, may occur in naturally deformed rocks at >300°C (Evans and Dunne, 1991).

In the present study, a broad distribution of coarse-grained carbonate rock specimens was studied in thin-section to interpret maximum deformation temperatures from microstructural assemblages. First appearances of diagnostic microstructures, as discussed by Burkhard (1993), were used to assign and map deformation temperatures.

2.2. Quartz microstructure geothermometry

Hirth and Tullis (1992) described microstructural assemblages developed experimentally in quartz-rich aggregates deformed over a range of temperatures and strain rates. This study demonstrated that quartz crystal plastic deformation (dislocation creep) and recovery mechanisms, and thus quartz microstructures, are strongly temperature dependent (Fig. 2), similar to those for calcite discussed above.

Based on standard petrographic and TEM analyses, Hirth and Tullis (1992) interpreted that three distinct deformation mechanism (dislocation creep) regimes operated to generate the suites of experimentally produced microstructures they observed. Regime-to-regime transitions in the experimentally deformed specimens involved both temperature and strain rate dependencies (Fig. 2). The characteristic microstructural assemblages for each of the three regimes, petrographic criterion for identifying them, and the regime

transitions are summarized from Hirth and Tullis (1992) below. Photomicrographs showing representative microstructures are presented below.

Regime 1: Deformation at relatively low temperatures or high strain rates produces irregular patchy extinction within originally undeformed detrital quartz grains. Along original grain boundaries some new, very fine (<1 μm), equant, recrystallized quartz grains may form. At low strain, these recrystallized grains are too small to be seen using a standard petrographic microscope, but at higher strain they may become visible.

Regime 2: At relatively moderate temperatures and moderate strain rates, relicts of original undeformed detrital quartz grains (i.e. quartz augen) can still be recognized. However, these relicts are commonly strained into abundant subgrains, which are generally about 1–10 μm in size. The subgrains in turn are generally replaced by relatively small, yet petrographically visible (>l μm), dynamically recrystallized grains, which are especially common along subgrain boundaries. Other petrographic features characteristic of Regime 2 include original grain relicts that are extremely flattened and form long quartz ribbons, and core and mantle textures.

Regime 3: At higher relative temperatures or lower relative strain rates, recovery-dominated quartz microstructures predominate. Quartz deformed under Regime 3 conditions is thus typically completely or almost completely dynamically recrystallized. Original detrital grain boundaries are generally no longer recognizable and rare if any relicts of original detrital quartz grains remain. Quartz ribbons are rare in Regime 3 because recrystallization recovery is so effective, and new recrystallized grains are generally quite large (>5–10 μm), commonly larger than the subgrains they replaced.

In the present study, we examined thin-sections from a broadly distributed suite of metaquartzite specimens. Quartz precipitated in pressure fibers is likely weaker than that of detrital quartz grains (see discussion in Microstructures and Deformation Mechanisms section). To avoid introducing bias into our analysis we describe, map, and compare quartz microstructures developed only from detrital quartz grains and in relicts (augen), not those in pressure fiber tails. We map the Regime 1–Regime 2 transition as the first appearance petrographically of subgrains and use the predominance of large (> 5–10 μm) recrystallized grains over subgrains to define the Regime 2–Regime 3 threshold. We make and present qualitative determinations on transitional specimens (e.g. Regime 1–2; Regime 2–1) based on the relative abundances of diagnostic microstructures.

2.3. Fission track analysis

Fission tracks are linear damage zones caused by the spontaneous fission of uranium atoms in U-bearing minerals such as zircon and apatite. A fission track age can be measured because ^{238}U decay occurs at a constant rate and the number of fission tracks per unit area, in conjunction with uranium concentration, gives a measure of the time since track accumulation began (Wagner and Van den Haute, 1992). The fission track age also depends on both the time interval of track retention and the amount of annealing that has occurred during that time (Green, 1988).

Progressive heating of the host mineral, apatite or zircon, for times of long duration ($\sim 10^6$ years) can cause fission tracks to anneal. If the temperature and duration of heating are of sufficient magnitude, all existing fission tracks in the mineral will be annealed and the fission track age will be completely reset. Below a certain critical temperature, referred to as the closure temperature (Dodson, 1973, 1979), fission tracks begin to accumulate. For apatite, the closure temperature for track retention is estimated to be 100 ± 20°C at geologic cooling rates of 1–10°C/my (Wagner, 1968; Naeser and Faul, 1969; Naeser, 1981; Gleadow and Duddy, 1981; Wagner and Van den Haute, 1992). Zircon has a higher estimated closure temperature for fission track retention, which is also dependent on cooling rate. Early zircon closure temperature estimates ranged from 175 ± 25°C (Harrison and McDougall, 1980) to 235–245°C for cooling rates of 10–30°C/my modeled by Brandon and Vance (1992) from annealing data of Zaun and Wagner (1985) and Tagami et al. (1990) and the closure temperature equations of Dodson (1979). Recent borehole data from the Vienna basin (Tagami et al., 1995), laboratory annealing data (Yamada et al., 1995), and natural annealing data from the contact metamorphic aureole around a granitic pluton (Tagami and Shimada, 1996), suggest a significantly higher temperature range for the zircon partial annealing zone, ~230 to 330°C, for times of $\sim 10^6$ years.

In this study, we present new fission track results from the analyses of five zircon specimens and one apatite specimen. Appendix A outlines the details of the laboratory analysis procedures. We combine these new data with the published zircon fission track results of Algar et al. (1998) in our analysis.

3. Structural geology

3.1. Western and central Northern Range (main body)

Rocks in the main body of the western and central Northern Range experienced three principal phases of deformation. The structures that formed during each deformation phase can be readily distinguished in outcrop and are summarized in Table 1a. Along the southern range front, mesostructures predating the late range front faults and shear bands (i.e. the D_3 structures discussed below) are, however, geometrically similar to those in the eastern Northern Range (see Table 1b eastern Northern Range section below). These pre-D_3 range front structures are described no further.

The earliest recognizable compositional layering in these

Table 1
Summary of deformation phases and structures[a]

(a) Western and Central Northern Range (main body)		
	S_0	Probable sedimentary bedding
		Locally parallels early mimetic (?) mica foliation
D_1	F_1	Tight to isoclinal
		Long accordion-like trains
		Sub-meter wavelengths
		Limbs highly attenuated
		Isolated hinges common
	S_1	Penetrative
		Schistose
		Approximately axial planar to F_1 mesofolds
		Transposes S_0
		Dips consistently <20–30° S
		South-dipping homocline
	L_1	Generally trends E–W
		Subhorizontal plunges
		Metaquartzite stretching lineations: long axes of stretched detrital quartz grains and fibrous quartz overgrowths
		Metacarbonates: generally only S_0–S_1 intersection lineations
D_2	F_2	Main body of range and north coast: recumbent mesofolds with consistent asymmetry and top–south vergence; hinges commonly parallel L_1
	S_2	Spaced pressure solution foliation locally well-developed
		Approximately axial planar to F_2 mesofolds
D_3		Main body of range and north coast: normal displacement shear bands and normal faults; strike roughly N–S; dip steeply toward the E and W; subhorizontal E–W principal extension
		Range front: normal faults and shear bands
(b) Eastern Northern Range E–W striking		
	S_0	Cross-bedding and graded bedding well-preserved
		Sedimentary layering easily recognizable in most outcrops
D_1	F_1	Generally symmetric, upright mesofolds
		NW–SE striking subvertical axial surfaces
		Subhorizontal hinges
	S_1	Spaced, slaty cleavage
		Dominant tectonic foliation in this part of the range
		Generally axial planar to F_1
	f_1	Uplimb thrusts on F_1 mesofolds
		Normal faults accommodated F_1 hinge-parallel stretching
D_2	F_2	Generally symmetric, recumbent mesofolds of S_1
		Mesofold trains in fault-bounded panels
		Detached from adjacent homoclinal panels of S_1
	S_2	Axial planar to F_2 mesofolds
		Substantial geometric variability
	f_2	Detachment faults (see F_2 above)
D_3	f_3	Range front: normal faults and shear bands
		Brittle faults in northeastern Northern Range according to Algar (1993)

[a] The D_i, S_i, F_i, and L_i nomenclature refers respectively to deformation phases, planar fabric (e.g. foliation, cleavage) elements, folds, and lineations in successive phases of deformation and successive generations of structures.

rocks locally parallels an early mica foliation, which probably represents original bedding in the sedimentary protoliths based on the absence of correlative mesofolds or microfolds, the general low metamorphic grade of these rocks, and the large variation in thickness of the individual early compositional layers (e.g. Passchier and Trouw, 1996, p. 59). We interpret this foliation as having resulted from the static mimetic recrystallization of clay minerals during sedimentary burial, rather than from tectonic shortening, and designate it S_0.

During the first and most ductile phase of deformation, D_1, S_0 was transposed into the S_1 tectonic foliation [see Turner and Weiss (1963, pp. 92–95) and Hobbs et al. (1976, pp. 252–264) for a general outline of the process of transposition]. S_0 is tightly to isoclinally folded at microscopic and mesoscopic scales. F_1 mesofolds generally have highly attenuated limbs, and commonly occur as isolated mesofold noses. S_1 is penetrative, schistose, and approximately axial–planar to F_1 mesofolds. Well-defined L_1 stretching lineations are generally present in metaquartzites, but not in metacarbonates. S_1 dips consistently and gently (<20–30°) southward, and forms a homocline in which resistant metasandstone layers protrude as hogbacks (Fig. 3). Correlative F_1 macrofolds have not been rigorously identified and mapped. Nonetheless, Potter (1973), Algar (1993), and Algar and Pindell (1993) present preliminary and highly over-simplified interpretations of the major folds in the range.

Late folds that deform S_1 are common, and may represent one or more deformation phases, which we collectively refer to as D_2. In the main body of the range and along the north coast, F_2 folds are systematically asymmetric, consistently indicating top–south vergence.

The youngest structures observed are normal displacement shear bands and normal faults related to a third deformation phase (D_3). These extensional shear bands and faults strike approximately north–south and dip toward the east and west in the main part of the range. Along the southern boundary of the range, early structures have been strongly overprinted by pervasive D_3 brittle faulting (Fig. 4a). Late shear bands with consistent ~80–85° southward dips and top–south normal offsets are also common along the range front (Figs. 4b and 5). The range-front faults have more diverse geometries and slip orientations (Fig. 4a) than the shear bands (Fig. 4b), and anastamose through complex cataclastic zones. The most through-going and systematic of these faults strike east–west, and dip steeply toward the north and south; many have dip-slip striae; some have down-dip slip indicators (Fig. 4a). The kilometer-scale cataclastic zones in which these faults occur are very distinctive, found only along the range front, and roughly coincide with Kugler's (1961) Arima fault trace (Fig. 1b; also see Kinematic range front fault models section). Together the range-front shear bands and systematic faults accommodated subhorizontal north–south principal extension.

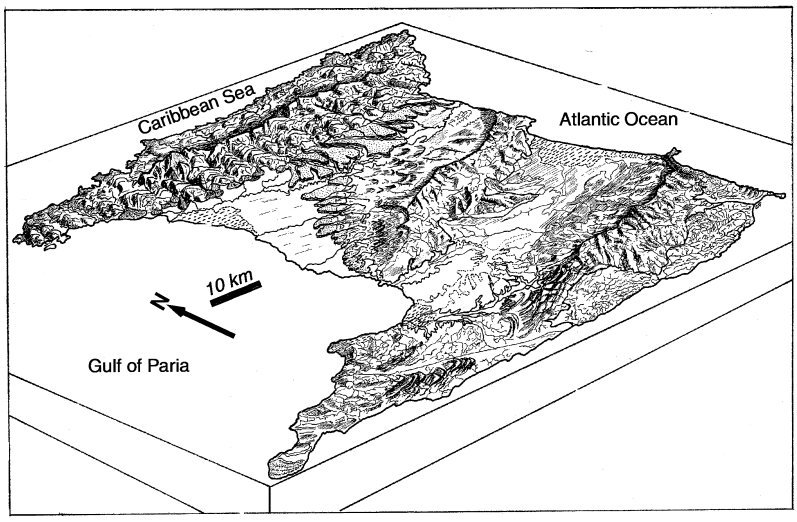

Fig. 3. Perspective cartoon sketch showing the principal geomorphic features of Trinidad. Redrawn by Colin Plank from Sutter (1960).

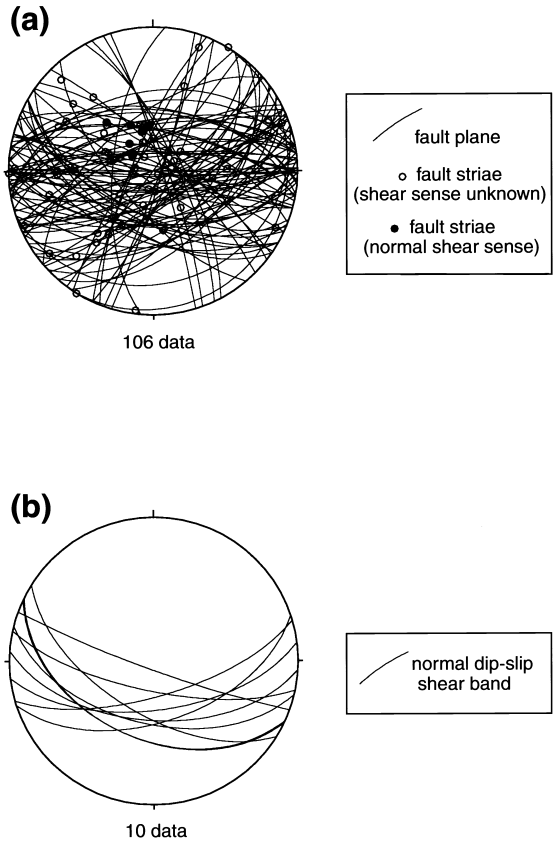

Fig. 4. Lower-hemisphere, equal-area plots showing structural data from the southern boundary (Arima fault zone) of the Northern Range: (a) slickenside striae (open and filled circles) and brittle fault planes from range-front (Arima) fault zone exposures at Champs Fleurs (Hilltop Road), St Joseph, and Lopinot, and (b) normal dip-slip extensional shear bands from scattered localities concentrated along the range front. All shear bands have down to the south, normal, dip-slip sense of displacement (see Fig. 5). See Fig. 1b for site locations.

3.2. Eastern Northern Range

Rocks in the eastern Northern Range, which were first mapped by Barr (1963), experienced two phases of folding, and two, or possibly three, major phases of fabric development (Table 1b; Algar, 1993; Algar and Pindell, 1993). Nonetheless, bedding (S_0), including cross-bedding and grading, is still well preserved in most outcrops.

The earliest (F_1) mesofolds are upright, and are accompanied by S_1, a spaced slaty cleavage. Symmetric and recumbent F_2 mesofold trains fold S_1 and generally occur in faultbounded panels, detached from adjacent homoclinal panels of S_1. Where an axial planar S_2 foliation is developed, it strikes NE–SW with vertical to horizontal dips and a complete spectrum of dip directions.

Mesoscopic brittle contractional and extensional faults are also common in the eastern part of the range. Some faults may be late (i.e. D_3), as suggested by Algar (1993) and Algar and Pindell (1993), but many that they ascribe to D_3 (e.g. at Tompire Bay), we interpret as uplimb thrusts that formed during F_1 folding, D_1 normal faults that accommodated F_1 hinge-parallel stretching, and D_2 detachments.

In the northeastern Northern Range, particularly near the villages of Toco and San Souci (Fig. 1b), the rocks and structures are quite different from those in the rest of the eastern Northern Range described above and summarized in Table 1b. The small body of basalt that crops out at Sans Souci (Barr, 1963; Fig. 1b) is the only igneous rock exposed in Trinidad; from it, Frey et al. (1988) identified minerals diagnostic of the prehnite-pumpellyite facies. Abundant faults, shear zones, and extensional fractures occur in these basalts, and according to Wadge and Macdonald (1985), may be due to both rapid cooling and later tectonism.

Algar (1993) first suggested that the rocks exposed near Toco comprise a tectonic melange of broken slate and metasandstone (also see Algar and Pindell, 1993). Late faulting

Fig. 5. Sketch from photograph of a south-dipping extensional shear band near the southern boundary of the Northern Range near Port-of-Spain (Fig. 1b). View looking subhorizontally toward the east. Drawn by Colin Plank.

and shearing in the melange is superposed on a D_1 fabric identical to that present across most of eastern Northern Range and described above. No detailed study of slip indicators on mesofaults in the Toco melange exists and thus the tectonic significance of this unit remains undetermined.

4. Microstructures and deformation mechanisms

4.1. Western and central Northern Range (main body)

Quartz-rich rocks of the western and central Northern Range contain pervasive S_1 and L_1 fabrics that are defined by a number of microfabric subelements. Microboudinage (ductile necking) of detrital quartz grains defines principal stretching and shortening directions, which are generally subparallel to those same directions defined by the long axes of tabular, pressure-solved, quartz augen, and quartz fibers that have grown in strain shadows around rigid pyrite grains and quartz augen (e.g. Fig. 6c, d). Together the ductilely stretched grains and pressure fiber tails make up the mesoscopic stretching lineations (L_1), which are well-defined in metaquartzites. Generally only S_0–S_1 intersection lineations occur in metacarbonates, probably because the metacarbonates are more fully recrystallized and recovered from D_1 crystal plastic strain than the metaquartzites.

New dynamically recrystallized quartz grains (Fig. 6b, d, e) with strong crystallographic preferred orientations are abundant in the metaquartzites. Crystallographic preferred orientations (CPOs) were determined for quartz *c*-axes for some of the most strongly recrystallized samples; two such CPO fabric plots are presented in Fig. 7. Well-developed cross-girdle and Y-maximum CPOs, probably indicative of dislocation creep (e.g. Law, 1990), are common.

The new recrystallized quartz grains described above are clearly related to the recovery of crystal plastic D_1 strain (see e.g. Etheridge and Wilkie, 1981; Law, 1990; Hirth and Tullis, 1992), but many have been partially dissolved by pressure solution (Fig. 6e). Consequently, these recrystallized grains commonly have modified truncated and tabular, rather than pristine and equant, shapes. The principal shortening and stretching directions for the pressure-solved recrystallized grains is generally subparallel to those same directions for the ductile D_1 fabric subelements discussed above.

M-domains, or p-bands, which according to Davis (1984), p. 407) and Cobbold et al. (1972), form by the accumulation of mica by intense pressure solution concentrated in spaced zones and subsequent recrystallization, comprise another common S_1 foliation subelement (e.g. Fig. 6e) in both metacarbonates and metaquartzites.

In summary, we interpret that S_1 and L_1 formed by pressure solution and quartz and calcite crystal plasticity acting simultaneously to take up D_1 strain.

Quartz in L_1 pressure fiber tails locally exhibits complete dynamic recrystallization of fibrous quartz, evidence of intense crystal plastic deformation. In contrast, neighboring detrital quartz grains and relicts (augen) may commonly have been only weakly strained via crystal plasticity with wavy extinction and subgrains (Fig. 6b). This is probably how the core and mantle textures, common in many metaquartzite specimens, developed. Quartz of pressure fiber origin thus appears weaker than detrital quartz, perhaps owing to a greater water content (Griggs and Blacic, 1965).

Grain truncation, resulting in the development of strong grain-shape fabrics, and the spaced nature of the S_2 cleavage, indicate a pressure solution origin. D_3 structures are clearly brittle and cataclastic. The microstructures described above therefore indicate that D_1 coincided

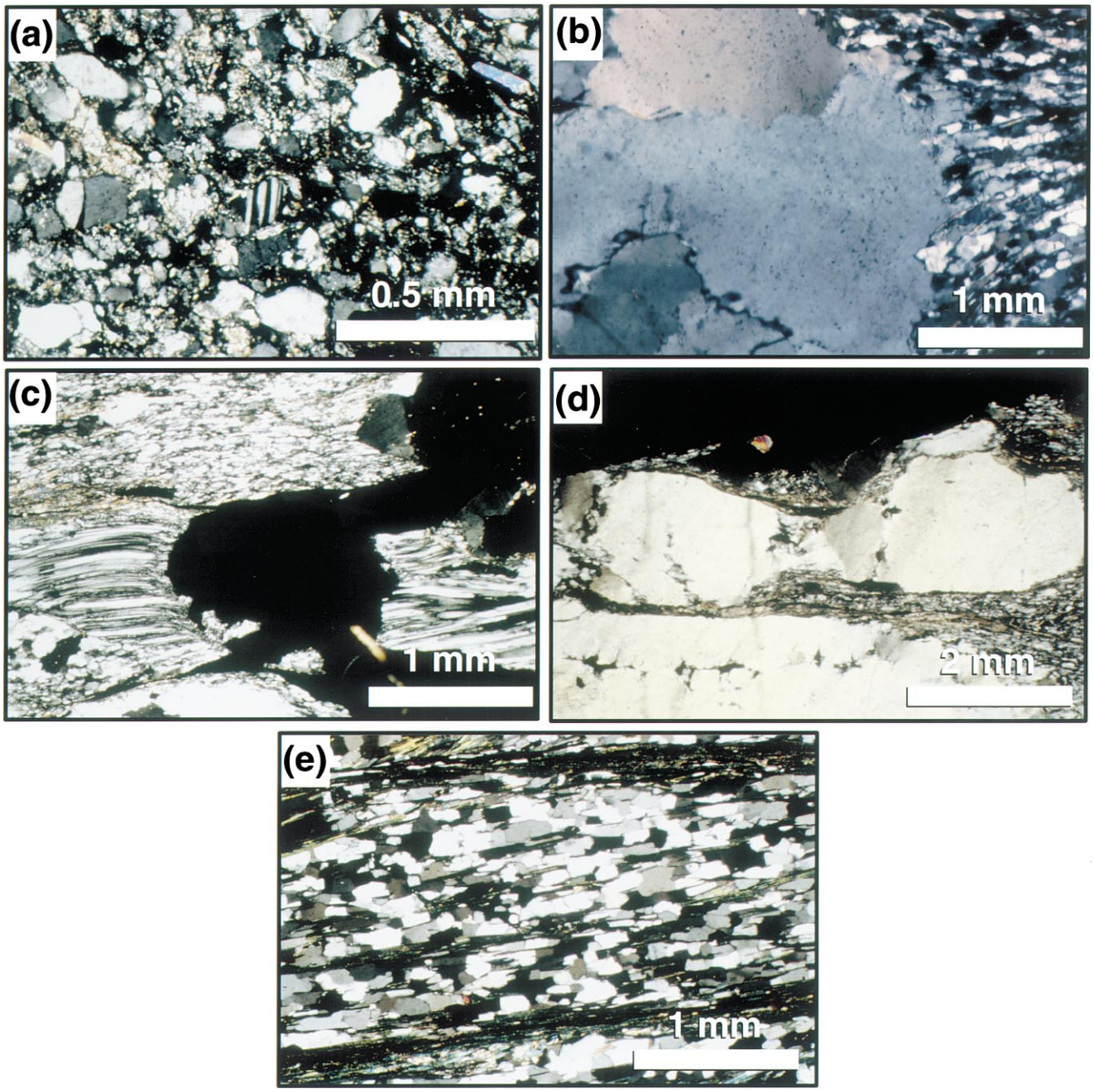

Fig. 6. Photomicrographs of quartz microstructures of the Northern Range: (a) Patchy extinction in Regime 1 quartz grains. Sample GR 94-1, northeastern Northern Range. (b) Relict detrital quartz grain with abundant subgrains and few new recrystallized grains along subgrain boundaries. Recrystallized quartz grains and mica flakes form tail on relict detrital grain. Thin section is cut parallel to mesoscopic stretching lineation. Sample Uphill from Hilltop, Regime 2. (c) Pristine quartz fibers preserved around an opaque iron oxide mineral grain. Quartz subgrains and small, recrystallized quartz grains in surrounding rock are Regime 2 microstructures. Thin section is cut parallel to mesoscopic stretching lineation. Sample Chupara Bay. (d) Ductilely stretched and necked relict detrital quartz grain. Subgrains and recrystallized grains, abundant in high-strain neck zone, indicate Regime 2. Thin section is cut parallel to mesoscopic stretching lineation. Sample Chupara Bay. (e) Regime 3 rock composed entirely of large (100–200 μm) dynamically recrystallized quartz grains. Sample Macq Bay. See Fig. 9c for sample locations.

roughly with peak grain scale ductility, and therefore, peak deformation temperature.

4.2. Eastern Northern Range

Most mineral grains in the eastern Northern Range experienced only minor shape changes. However, evidence for locally high strain is present (e.g. across spaced S_1 and S_2 slaty cleavage planes). Quartz grains generally have undulatory or patchy extinction, and also some subgrains, indicating that they have experienced some crystal plastic strain (Fig. 6a). Calcite grains are mechanically twinned

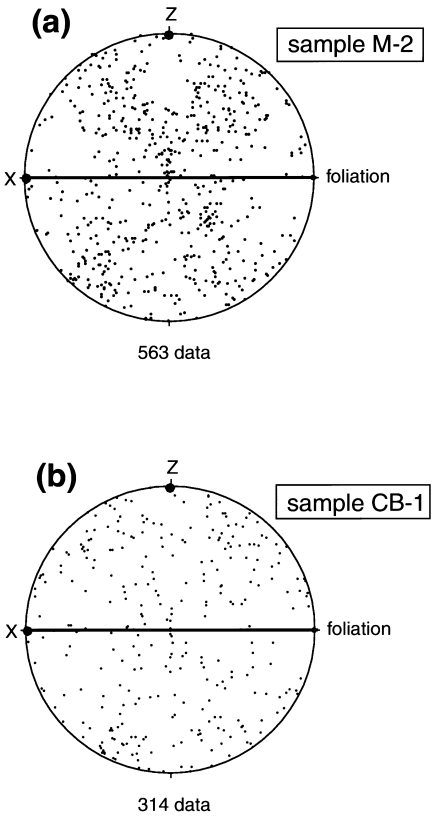

Fig. 7. Lower-hemisphere, equal-area, quartz c-axis fabric scatter plots for two strongly recrystallized metaquartzite samples: (a) M-2 (Regime 2–3), and (b) CB-1 (Regime 2–3). X and Z are principal finite strain directions determined from mesoscopic stretching lineation and foliation. See Fig. 9c for sample locations.

indicating that they, too, have been ductilely strained (e.g. Fig. 8c). However, in general ductile strain has not been recovered by recrystallization.

Original quartz grain shapes are generally only slightly modified by dissolution. Short, and also commonly multi-directional, quartz fibers also indicate that pressure solution strain is generally low.

Algar and Pindell (1993) report a complete lack of early, "ductile", D_1 fabric elements from the Sans Souci basalt, and attribute this to late (post-D_1) tectonic emplacement of a Toco–Sans Souci allocthon. Alternatively, the lack of a D_1 fabric may reflect that those basaltic minerals have higher crystal plastic threshold temperatures than those of the calcite- and quartz-bearing in the surrounding metasedimentary rocks (also see Discussion and Conclusions section below).

5. Geothermometry results

5.1. Calcite microstructure geothermometry

The degree of deformation of the Northern Range carbonates varies from weakly deformed limestone, in which grain-scale sedimentary fabrics are preserved, to carbonate schist in which grain-scale sedimentary fabrics have been completely overprinted (Fig. 8). Calcite microstructural assemblages indicate significant lateral variations in deformation temperatures (Fig. 9a).

Microstructures from the carbonate schists in the northwestern Northern Range record the highest calcite deformation temperatures. These rocks are nearly completely dynamically recrystallized and typically recrystallization has obliterated their original sedimentary fabrics. These samples are thus interpreted to have been deformed at >300°C. An upper temperature boundary of 400°C can be assigned to this (Type V) microstructural assemblage based on the maximum metamorphic temperatures of 300–400°C estimated by Frey et al. (1988).

Samples from the eastern and southwestern parts of the range have preserved sedimentary fabrics. In these rocks, twinning accommodated the bulk of crystal plastic strain. Lateral variations in twin morphology indicate that maximum deformation temperatures decrease eastward and southward from >300°C in the northwestern Northern Range, to 200–250°C in the northeastern Northern Range, and to 150–200°C along the southwestern edge of the range.

5.2. Quartz microstructure geothermometry

Lateral variations in quartz microstructures also reflect a systematic east-to-west increase in deformation temperatures (Fig. 9c). In the northwestern and western Northern Range, coarsely recrystallized Regime 3 quartz 'mylonites' crop out. These rocks record the relatively highest temperatures of quartz deformation. In the northeastern part of the range quartz-rich metasedimentary rocks contain relatively low-temperature Regime 1 and transitional Regime 1–2 quartz microstructures. Some samples in the northeast are, however, resedimented quartz aggregates (Fig. 9c; samples SS-94-1, SS-94-3) that were possibly derived from exposed Northern Range metasedimentary rocks. The mix of microstructures in the clasts in these rocks spans the entire spectrum of Regime types; regime designations are thus not meaningful. Quartz-bearing metasedimentary rocks across much of the remainder of the range contain predominantly Regime 2 microstructures, indicating relatively moderate deformation temperatures.

5.3. Fission tracks

The zircon and apatite fission track ages determined in this study are given in Table 2; locations are shown in Fig. 9b and given in Table 3. Three samples (LOP-93, Mat-m, and Blanch-3) yielded young zircon fission track ages, ranging from 12 ± 2 to 22 ± 3 Ma, with tightly clustered, unimodal, single-grain age distributions (Table 2). We interpret that the zircon fission track ages for these samples are reset and represent the time at which the host rocks cooled through the zircon closure temperature range of ~230–330°C.

Two samples, GP-1 and Ar-17, yielded significantly older

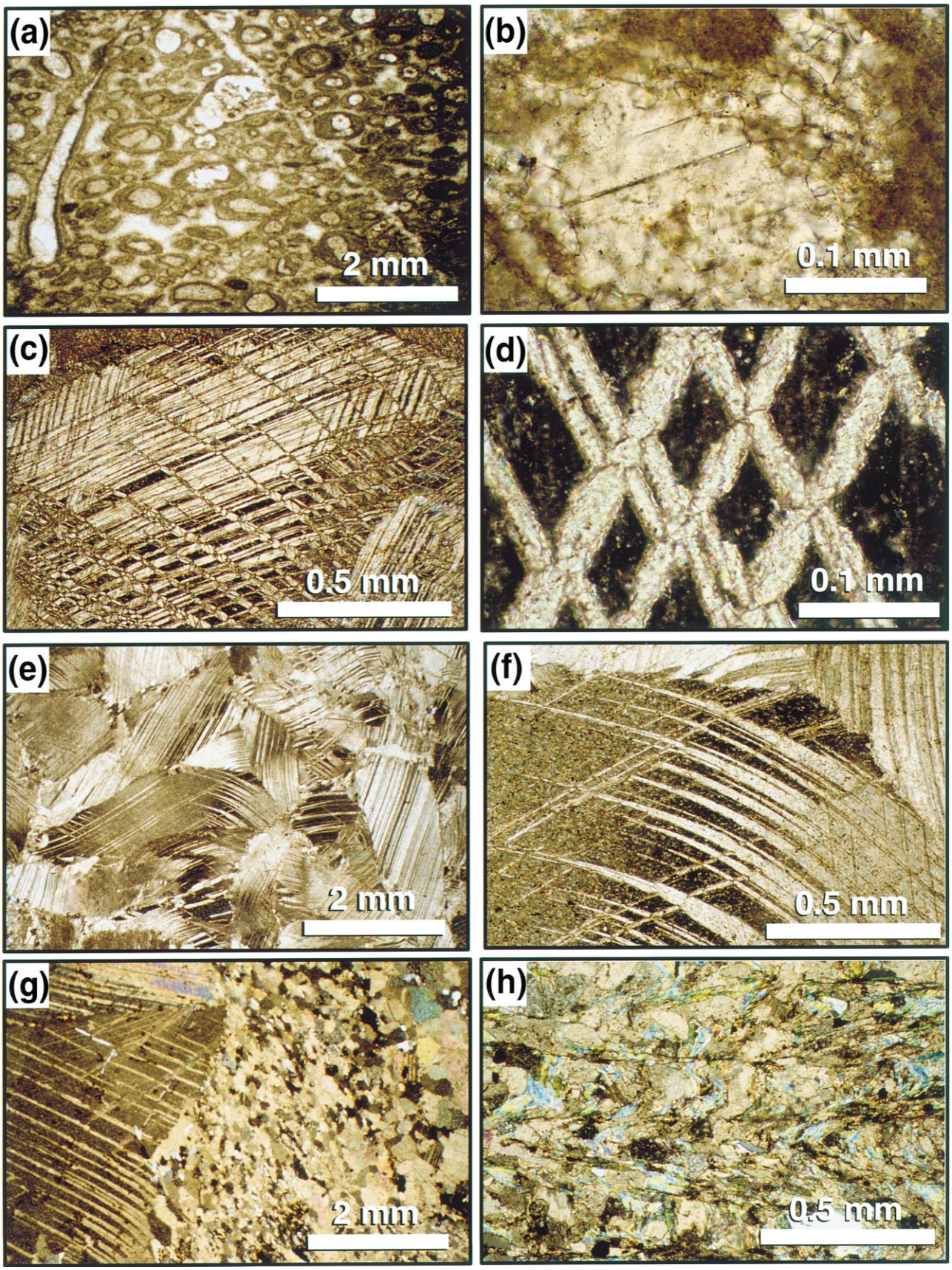
(a)
2 mm
(b)
0.1 mm
(c)
0.5 mm
(d)
0.1 mm
(e)
2 mm
(f)
0.5 mm
(g)
2 mm
(h)
0.5 mm

zircon fission track ages 84 ± 13 Ma and 172 ± 32 Ma, respectively. We interpret these zircon fission track ages as detrital ages because they are both older than their protolith depositional age range (~150–67 Ma; Tithonian to Maastrichtian). The single-grain age distributions are broad with a high percentage of old grain ages, especially in sample GP-1 (Table 2). These data suggest that samples GP-1 and Ar-17 have never been heated above the top of the zircon fission track partial annealing zone (PAZ) temperature of ~230°C. Therefore, their zircon fission track ages represent the fission track ages of their clastic source terrane and they are unreset.

All of the samples in this study gave extremely poor apatite yields. Only one apatite fission track age (22 ± 4 Ma for sample GP-1) was obtained (Fig. 9b; Table 2). This apatite fission track age is a weighted mean age from three separate apatite mounts (GP-1A, GP-1B, GP-1C; Table 2) within the same irradiation tube. The three individual apatite fission track ages are within one sigma error of each other as follows: 15 ± 8 Ma, 23 ± 10 Ma, and 23 ± 5 Ma. The weighted mean apatite fission track age of 22 ± 4 Ma is significantly younger than the depositional age of the protolith formation at Galera Point and is thus considered reset. Note that the same sample, GP-1, yielded a detrital zircon fission track age. The rocks at Galera Point were thus heated to temperatures > 100 ± 20°C (apatite fission track closure temperature) for times of > 1 Ma, but not to temperatures > 230°C (top of zircon PAZ). Sample GP-1 cooled through 100 ± 20°C at 22 ± 4 Ma. No confined track length measurements, to further constrain cooling histories, were made because of the paucity of apatite grains.

6. Discussion and conclusions

We resolved differences in deformation temperatures across the Northern Range using three independent techniques: calcite microstructural geothermometry, quartz microstructural geothermometry, and fission track dating. Deformation temperatures reached a maximum of 300–400°C in the northwestern Northern Range, where both calcite and quartz are completely dynamically recrystallized, and zircon fission track ages were reset at ~12 Ma. Rocks in the northeastern part of the range have non-reset zircon fission tracks, reset apatite fission tracks, Regime 1 and Regime 1–2 and 2–1 quartz microstructures, and type III calcite twins; collectively these features represent deformation temperatures of 200–330°C. These results show that in general deformation temperatures in the Northern Range increase along an east-to-west trend. Type I to type II calcite twins from near the range's southern boundary indicate the lowest deformation temperatures, 150–200°C.

$^{40}Ar/^{39}Ar$ results presented by Foland et al. (1992a), and Foland and Speed, (1992b) (also R.C. Speed and K.A. Foland, 1990–1992, personal communications and unpublished data) corroborate the east-to-west thermal gradient documented in this study. Whole rock specimens analyzed from the northwestern Northern Range yielded ~25 Ma near-plateau $^{40}Ar/^{39}Ar$ ages, probably reflecting argon degassing from coarse metamorphic white mica from m-domains. $^{40}Ar/^{39}Ar$ analyses from the southern and northeastern parts of the range yielded more convoluted spectra with older total gas ages. These complex spectra probably reflect argon degassing from several sources, including old, detrital micas that were not heated to temperatures significantly above white mica blocking temperatures (~350°C).

Our results do not allow us to resolve whether the westward increase in thermal grade is abrupt across the Grand Riviere fault (Fig. 1b). They permit the interpretation that throw across this inferred fault may be either insignificant or nonexistent and that the observed grade change is mostly transitional. Another possibility is that the major east–west break in grade occurs nearer the center of the range (see Fig. 9b and Section 6.1 below). We speculate that a subhorizontal detachment fault or complex transition zone may separate an upper tectonic domain with relatively low deformation temperatures and predominantly upright D_1 fabrics from a lower tectonic domain with relatively high deformation temperatures and subhorizontal D_2 fabrics. Similar detachments and transition zones separate the infrastructure from the suprastructure in the Pyrenees (e.g. Carreras and Capela, 1994, 1995; Aerden, 1995; Garcia-Sansegunto, 1996; and references therein). Rocks with relatively low deformation temperatures and upright fabrics, perhaps also part of the upper domain, also occur in what are likely down-dropped normal fault blocks along the southern boundary of the Northern Range (see Kinematic range front fault models section below).

Our results do not require the Sans Souci basalt (Fig. 1b) to be allocthonous as suggested by Algar and Pindell (1993). Frey et al. (1988) report prehnite–purnpellyite minerals from these rocks, the stability field of which ranges from ~2–7 kb and ~100–300°C (Spears, 1993). These temperatures overlap with those that we obtain from the calcite microstructures (200–250°C) and the unreset zircon fission track ages (<230–330°C) in the surrounding metasedimentary rocks.

Fig. 8. Photomicrographs of microstructures in carbonate rocks of the Northern Range: (a) Sedimentary texture preserved in sample PG-94-5, (b) thin and thick twins in calcite cement from Cronstadt Island, (c) crossing thick twins and nearly completely twinned calcite grain in sample GR-94-3, (d) cross-cutting thick twins in calcite cement in sample PG-94-8, (e) curved thick twins in calcite vein in sample PG-94-8, (f) detail of curved and tapering thick twins in sample PG-94-8 shown in (e), (g) discontinuous, patchy twins and recrystallized grains in carbonate schist from Maraval Pit sample, (h) crenulation fabric developed in cm-scale isoclinal fold in carbonate schist from Santa Cruz quarry. See Fig. 9a for sample locations and microstructural assemblage (twin type) designations.

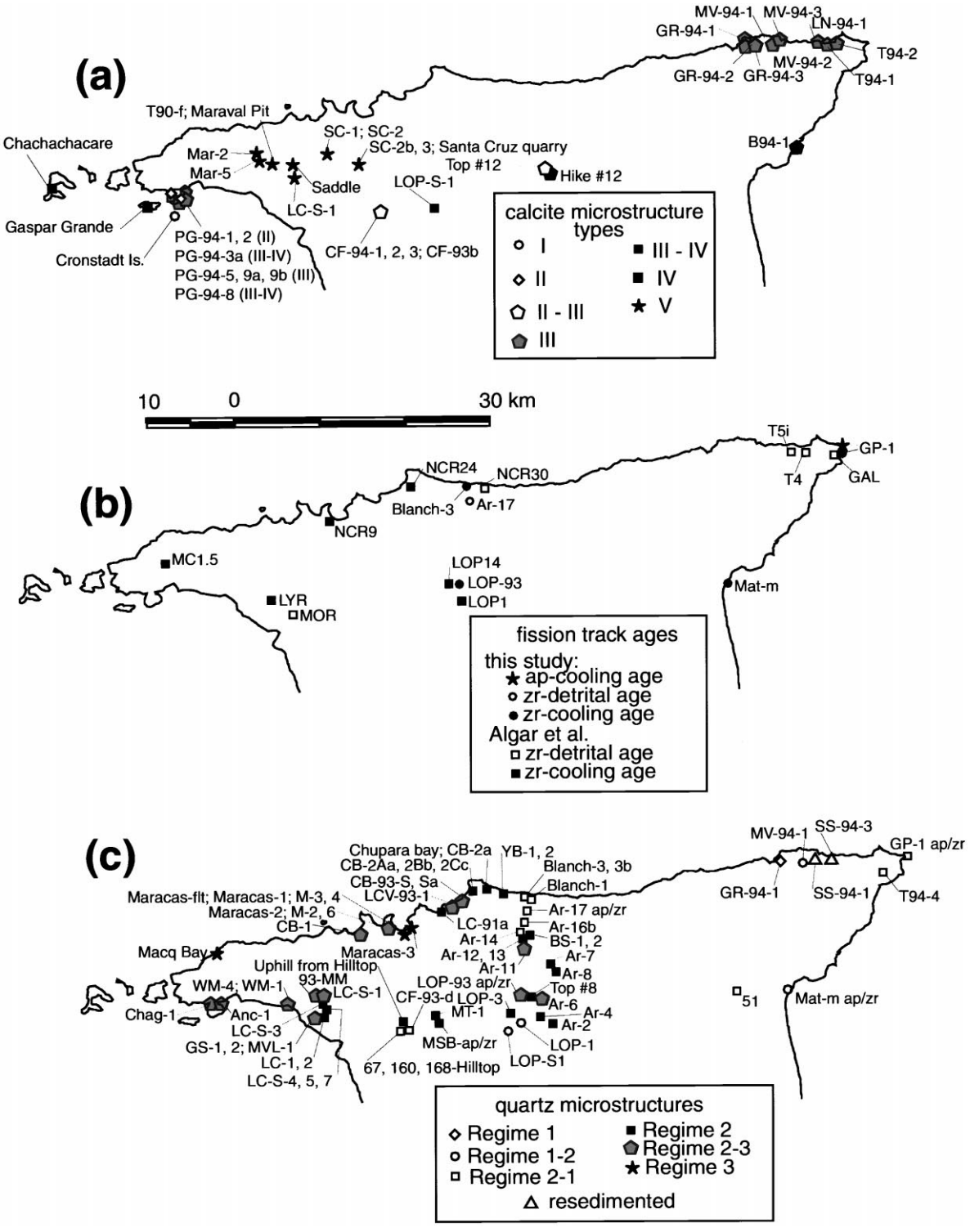

Fig. 9. (a) Map of the Northern Range showing the distribution of calcite microstructural types (I–V). Types I–IV coincide with Burkhard's (1993, Fig. 6) twin types I–IV. Type V refers to completely recrystallized carbonate rocks. Deformation temperatures inferred from each type are: I (<200°C), II (>l500°C, < 250°C), III (>200°C, <250°C), IV (>250°C), and V (>300°C). (b) Map of the Northern Range showing apatite (ap) and zircon (zr) fission track cooling (reset) versus detrital (unreset) age determinations from this study and from that of Algar et al. (1998). See Table 2 for sample ages. (c) Map of the Northern Range showing the distribution of quartz microstructural Regimes (1–3). No microstructural regime determinations were made for resedimented quartz aggregates SS-94-1 and SS-94-3 (see Geothermometry Results section).

Table 2
Zircon (ZFT) and apatite fission (AFT) track ages[a]

Sample	ZFT age (Ma)	± 95% confidence	No. of grains	U (p.p.m.)	$P(\chi^2)$%	AFT age (Ma)	± 95% confidence	No. of grains	U (p.p.m.)	$P(\chi^2)$%
LOP-93	12.0	+ 1.7-1.5	20	202.4	1.9					
Mat-m	19.4	+ 3.7-3.1	13	144.8	1.2					
Blanch-3	22.1	+ 4.7-3.8	8	180.3	99.3					
Ar-17	172.3	+ 34.0-28.5	14	230.5	93.4					
GP-1A	83.7	+ 14.3-12.3	17	190.2	1.3	15.3	+ 24.1-11.4	3	10.2	100
GP-1B	ND					23.9	+ 53.5-8.3	1	24.0	ND
GP-IC	ND					23.5	+ 13.1-9.3	3	15.4	5.3
LYR*	11.9	± 1.0	11		30					
NCR24*	15.4	± 1.2	10		29					
NCR30*	271	± 42	4		100					
LOP14*	11.3	± 1.3	9		6					
LOP1*	11.8	± 1.3	8		100					
MC1.5*	11.7	± 0.9	11		4					
MOR*	205	± 18.1	8		0					
NCR9*	11.1	± 0.6	20		0.9					
T5i*	202	± 16	9		3					
T4*	121	± 7.2	11		9					
GAL*	116	± 9	10		0.1					

[a] Apatite and zircon FT ages given as χ^2 ages (Brandon, 1992). Apatite zeta = 103.4 ± 2.3 for CN1 glass (MR-T) and zircon zeta = 344.5 ± 18.7 for CN_1 glass (MR-T). Samples marked (*) from Algar et al. (1998) filtered data set (see Section 6.1). Weighted mean AFT age for GP-1 from subsamples GP-1A, GP-1B, and GP-1C = 22.5 ± 9.2 Ma for seven grains.

6.1. Rock exhumation rate estimates

Our new zircon fission track ages and those of Algar et al. (1998) (Fig. 9b) allow subdivision of the Northern Range into three thermal domains, and estimation of rock exhumation rates in each domain. We filtered the 'noisy' data set of Algar et al., (1998) (see also Algar, 1993) by excluding problematic "partially reset" samples with mixed Neogene and older ages and also broadly mixed Neogene ages. The filtered data are listed in Table 2. In the western part of the range, our ages and the filtered ages of Algar et al. are statistically identical at two-sigma error, and in many cases, samples from the two studies are statistically identical at one-sigma error. These western rocks all cooled through ~230°C nearly simultaneously at ~12 Ma. Rocks in the northeastern Northern Range were never heated to > 230–330°C based on their detrital zircon fission track ages. In the central part of the range, some rocks cooled through the zircon PAZ of 230–330°C at ~22 Ma (e.g. Blanch-3, Mat-m), whereas others (e.g. Ar-17, NCR30) were never heated to >230–330°C and yielded detrital zircon FT ages. Details regarding the boundary between rocks with detrital and reset zircon FT ages in the central Northern Range are currently lacking. Rocks with reset zircon FT ages are included in the central domain, those with unreset zircon FT ages are placed in the eastern domain. That many of the ~22 Ma central domain ages overlap with many of the ~12 Ma western domain ages at two-sigma error suggests that the boundary between these two domains may be gradational. Alternatively, rocks with unreset zircon FT ages along the north coast may occur in a block down-dropped along steeply dipping, N–S-striking, normal faults, akin to those we observed at the mesoscopic scale (Table 1a). Another possibility is that these 'cold' rocks occur as a non-eroded patch of eastern-domain-type rocks that are bounded at their base by a subhorizontal detachment fault (see the general Discussion and Conclusions section above).

We calculate average cooling and rock exhumation rates for each of the three thermal domains discussed above using the following assumptions: (1) a surface temperature today of 25°C, (2) a uniform zircon closure temperature of 275°C, (3) an apatite closure temperature of 100°C, (4) a 25°C/km geothermal gradient to convert the cooling rates to exhumation rates, (5) no isotherm advection during exhumation, and (6) steady exhumation. According to Mancktelow and Grasemann (1997), isotherms are probably not advected during relatively slow (<1 mm/year) exhumation; the exhumation rates calculated below are all < 1 mm/year. Steady exhumation is assumed simply because we generally have too few data to do otherwise. In the western domain, where we have sufficient data to asses whether exhumation was steady or not, it appears slightly faster from 12 Ma to today than from 25 to 12 Ma (Fig. 10).

Our estimated cooling and rock exhumation rates are 13.2°C/my and 0.53 mm/y for the western domain, 9.3°C/my and 0.37 mm/y for the central domain, and 3.4°C/my and 0.14 mm/y for the eastern domain. Like thermal grade, these values also increase systematically from east to west across the range (Fig. 10).

6.2. Kinematic range front fault models

The two exhumation processes that remove material from Earth's surface and allow rock from depth to be

Table 3
Sample locations[a]

Sample name	Rock type	Sheet	Local UTM	X	Y	Latitude (°W)	Longitude (°N)
51	metasandstone	16	PS 093 821	709300	1182100	61.08644	10.6884
160-Hilltop	metasandstone	13	PS 725 784	672500	1178400	61.42297	10.65682
168-Hilltop	metasandstone	13	PS 725 784	672500	1178400	61.42297	10.65682
67-Hilltop	metasandstone	13	PS 725 784	672500	1178400	61.42297	10.65682
93-MM	metasandstone	13	PS 622 826	662200	1182600	61.51693	10.69526
Anc-1	metasandstone	12	PS 504 809	650400	1180900	61.62486	10.68038
Ar-11	metasandstone	14	PS 851 863	685100	1186300	61.30741	10.72764
Ar-12	metasandstone	14	PS 849 866	684900	1186600	61.30922	10.73037
Ar-13	metasandstone	14	PS 845 872	684500	1187200	61.31285	10.73581
Ar-14	metasandstone	14	PS 830 885	683000	1188500	61.3265	10.74764
Ar-16b	metasandstone	4	PS 853 901	685300	1190100	61.30539	10.76199
Ar-17	metasandstone	4	PS 834 931	683400	1193100	61.32261	10.78921
Ar- 17/ap/zr	metasandstone	4	PS 834 931	683400	1193100	61.32261	10.78921
Ar-2	metasandstone	14	PS 877 781	687700	1178100	61.28406	10.65338
Ar-4	metasandstone	14	PS 869 789	686900	1178900	61.29133	10.66065
Ar-6	metasandstone	14	PS 868 813	686800	1181300	61.29213	10.68236
Ar-7	metasandstone	14	PS 868 832	686800	1183200	61.29203	10.69953
Ar-8	metasandstone	14	PS 867 844	686700	1184400	61.29288	10.71039
B-94-1	metacarbonate	16	QS 193 856	719300	1185600	60.99485	10.71946
Blanch-3	metasandstone	4	PS 819 947	681900	1194700	61.32711	10.80322
Blanch-1	metasandstone	4	PS 839 939	683900	1193900	61.31800	10.79641
Blanch-3b	metasandstone	4	PS 819 947	682900	1194600	61.32711	10.80322
BS-1	metasandstone	14	PS 845 872	681900	1194700	61.31284	10.73852
BS-2	metasandstone	14	PS 843 874	684300	1187400	61.31467	10.73763
CB-1	metasandstone	3	PS 669 904	666900	1190400	61.47361	10.76558
CB-2a	metasandstone	4	PS 787 954	678700	1195400	61.36547	10.81023
CB-93-S	metasandstone	4	PS 779 936	677900	1193600	61.37288	10.79399
CB-93-Sa	metasandstone	4	PS 779 936	677900	1193600	61.37288	10.79399
CB2-Aa	metasandstone	4	PS 785 943	678500	1194300	61.36736	10.80029
CB2-Bb	metasandstone	4	PS 785 943	678500	1194300	61.36736	10.80029
CB2-Cc	metasandstone	4	PS 785 943	678500	1194300	61.36736	10.80029
CF-93-b	metacarbonate	13	PS 727 783	672700	1178300	61.42114	10.65591
CF-94-1	metacarbonate	13	PS 727 783	672700	1178300	61.42114	10.65591
CF-94-2	metacarbonate	13	PS 727 783	672700	1178300	61.42114	10.65591
CF-94-3	metacarbonate	13	PS 727 783	672700	1178300	61.42114	10.65591
Chachachacare	metacarbonate	11	PS 360 815	636000	1181500	61.7528	10.6852
Chag-1	metasandstone	12	PS 479 812	647900	1181200	61.64771	10.68319
Chupara Bay	metaconglom	4	PS 787 954	678700	1195400	61.36547	10.81023
Cronstadt	metacarbonate	12	PS 497 784	649700	1178400	61.63136	10.6578
Gaspar Grande	metacarbonate	12	PS 470 793	647000	1179300	61.65601	10.66605
GP-1-ap/zr	metasandstone	6	QS 284 983	728400	1198300	60.91088	10.8337
GR-94-1	metacarbonate	6	QS 137 975	713700	1197500	61.04533	10.82735
GR-94-1	metasandstone	6	QS 137 975	713700	1197500	61.04533	10.82735
GR-94-2	metacarbonate	6	QS 133 977	713300	1197700	61.04898	10.82918
GR-94-3	metacarbonate	6	QS 141 974	714100	1197400	61.04168	10.82643
GS-1	metasandstone	13	PS 615 807	661500	1180700	61.52341	10.67811
GS-2	metasandstone	13	PS 615 807	661500	1180700	61.52341	10.67811
Hike #12	metacarbonate	15	PS 915 836	691500	1183600	61.24905	10.70291
LC-1	metasandstone	13	PS 619 802	661900	1180200	61.51977	10.67357
LC-2	metasandstone	13	PS 619 802	661900	1180200	61.51977	10.67357
LC-91a	metasandstone	4	PS 757 921	675700	1192100	61.39307	10.78054
LC-S-1	metasandstone	13	PS 624 816	662400	1181600	61.51514	10.68621
LC-S-3	metasandstone	13	PS 624 814	662400	1181400	61.51515	10.6844
LC-S-4	metasandstone	13	PS 625 811	662500	1181100	61.51425	10.68168
LC-S-5	metasandstone	13	PS 625 809	662500	1180900	61.51426	10.67987
LC-S-7	metasandstone	13	PS 623 807	662300	1180700	61.51609	10.67807
LCV-93-1	metasandstone	4	PS 766 927	676600	1192700	61.38481	10.78592
LN-94-1	metacarbonate	6	QS 216 982	721600	1198200	60.97306	10.83321
Lop-1	metasandstone	24	PS 828 775	682800	1177500	61.32887	10.6482
Lop-3	metasandstone	14	PS 826 794	682600	1179400	61.33061	10.66539
LOP-93	metasandstone	14	PS 836 821	683600	1182100	61.32133	10.68975
LOP-93 ap/zr	metasandstone	14	PS 836 821	683600	1182100	61.32133	10.68975

Table 3 (*continued*)

Sample name	Rock type	Sheet	Local UTM	X	Y	Latitude (°W)	Longitude (°N)
Lop-S-1	metacarbonate	24	PS 818 770	681800	1177000	61.33804	10.64373
M-2	metasandstone	3	PS 699 902	669900	1190200	61.44619	10.76363
M-3	metasandstone	3	PS 717 896	671700	1189600	61.42976	10.75812
M-4	metasandstone	3	PS 717 896	671700	1189600	61.42976	10.75812
M-6	metasandstone	3	PS 699 902	669900	1190200	61.44619	10.76363
Macq Bay	metasandstone	12	PS 508 873	650800	1187300	61.62094	10.73823
Mar-2	metacarbonate	13	PS 621 849	662100	1184900	61.51774	10.71606
Mar-5	metacarbonate	13	PS 619 851	661900	1185100	61.51956	10.71788
Maracas-1	metasandstone	3	PS 717 896	671700	1189600	61.42976	10.75812
Maracas-2	metasandstone	3	PS 699 902	669900	1190200	61.44619	10.76363
Maracas-3	metasandstone	3	PS 721 898	672100	1189800	61.42609	10.75991
Maracas-flt	metasandstone	3	PS 717 896	671700	1189600	61.42976	10.75812
Maraval Pit	metacarbonate	13	PS 624 846	662400	1184600	61.51501	10.71333
Mat-m	metasandstone	16	QS 151 824	715100	1182400	61.03342	10.69078
Mat-m ap/zr	metasandstone	16	QS 151 824	715100	1182400	61.03342	10.69078
MSB-ap/zr	metasandstone	14	PS 749 792	674900	1179200	61.40099	10.66395
MT-1	metasandstone	14	PS 753 804	675300	1180400	61.39728	10.67478
MV-94-1	metacarbonate	6	QS 161 972	716100	1197200	61.02341	10.8245
MV-94-2	metacarbonate	6	QS 162 972	716200	1197200	61.0225	10.8245
MV-94-3	metacarbonate	6	QS 173 976	717300	1197600	61.01241	10.82805
MVL-1	metasandstone	13	PS 615 808	661500	1180800	61.5234	10.67901
PG 94-8	metacarbonate	12	PS 501 804	650100	1180400	61.62763	10.67587
PG-94-1	metacarbonate	12	PS 514 801	651400	1180100	61.61576	10.67311
PG-94-2	metacarbonate	12	PS 515 801	651500	1180100	61.61484	10.6731
PG-94-3a	metacarbonate	12	PS 511 801	651100	1180100	61.6185	10.67312
PG-94-5	metacarbonate	12	PS 506 802	650600	1180200	61.62307	10.67404
PG-94-9a	metacarbonate	12	PS 503 806	650300	1180600	61.62579	10.67767
PG-94-9b	metacarbonate	12	PS 503 806	650300	1180600	61.62579	10.67767
Saddle	metacarbonate	13	PS 643 849	664300	1184900	61.49762	10.71596
Santa Cruz quarry	metacarbonate	13	PS 691 846	669100	1184600	61.45376	10.71304
SC- 1	metacarbonate	13	PS 662 850	666200	1185000	61.480258	10.71678
SC-2	metacarbonate	13	PS 662 850	666200	1185000	61.48025	10.71678
SC-2b	metacarbonate	13	PS 691 846	669100	1184600	61.45376	10.71304
SC-3	metacarbonate	13	PS 691 846	669100	1184600	61.45376	10.71304
SS-94-1	metasandstone	6	QS 186 986	718600	1198600	61.00047	10.83701
SS-94-3	metasandstone	6	QS 197 983	719700	1198300	60.99043	10.83423
T-90-f	metacarbonate	13	PS 624 846	662400	1184600	61.51501	10.71333
T-94-1	metacarbonate	6	QS 235 980	723500	1198000	60.9557	10.83129
T-94-2	metacarbonate	6	QS 242 983	724200	1198300	60.94928	10.83396
T-94-4	metasandstone	6	QS 252 967	725200	1196700	60.94024	10.81944
Top #12	metacarbonate	15	PS 917 841	691700	1184100	61.24719	10.70742
Top #8	metasandstone	14	PS 847 812	684700	1181200	61.31133	10.68156
Uphill from Hilltop	metasandstone	13	PS 724 787	672400	1178700	61.42387	10.65954
WM-1	metasandstone	13	PS 583 908	658300	1180800	61.55265	10.67915
WM-4	metasandstone	13	PS 583 808	658300	1180800	61.55265	10.67915
YB-1	metasandstone	4	PS 807 948	680700	1194800	61.34721	10.80471
YB-2	metasandstone	4	PS 805 948	680500	1194800	61.34904	10.80472

[a] Sheet numbers refer to Trinidad 1: 25 000 topographic sheet numbers. Local *x, y* coordinates are in UTM Zone 20.

brought closer to Earth's surface are erosion and normal faulting. Summerfield and Hulton (1994) report a world high erosional denudation rate of 0.7 mm/year for the Brahmaputra River basin, which drains the Himalayas. Their mean from the 30 globally distributed drainage basins is an order of magnitude lower, 0.07 mm/year. Milliman and Syvitski (1992) report that locally erosion rates can reach ~1 mm/year along small mountainous streams. Thus a tectonic contribution is probably not required to produce exhumation rates of the magnitude that we observe in the Northern Range. However, the southern range front is probably bounded by a major normal fault, discussed below, that probably played some role in differentially exhuming the Northern Range rocks. We model the differential Northern Range exhumation rates as if it was solely due to differential movement on a range-front normal-fault system. We then discuss observations which suggest that erosion was probably also an important contributing factor, albeit difficult to quantify.

A variety of kinematic models have been proposed for the fault bounding the Northern Range along its southern edge. Based on detailed geological mapping, Kugler, (1961)

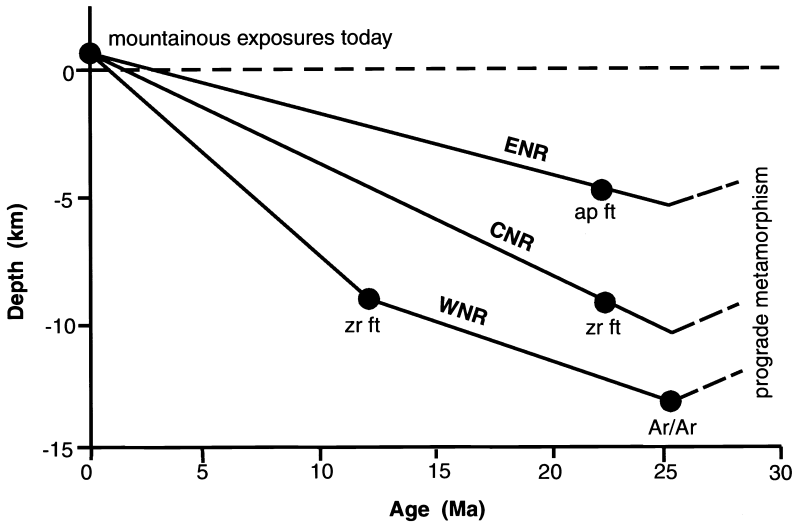

Fig. 10. Cartoon-graph showing approximate exhumation rates for the three thermal domains in the Northern Range as defined in this study: ENR—eastern, CNR—central, and WNR—western. Note that the total exhumation and the Neogene exhumation rate determined for the western Northern Range are double those values from the eastern part of the range. Data shown on the graph are: ap ft (apatite fission track, this study), zr ft (zircon fission track, this study and Algar et al. (1998)), and Ar/Ar ($^{40}Ar/^{39}Ar$, Foland et al., 1992a).

proposed that the range is bounded by a major south-dipping normal fault, which he named the Arima fault. Later interpretations based on plate-scale thinking speculated that the southern boundary fault is a north-dipping thrust (Speed, 1985), or a vertical strike-slip fault (Robertson and Burke, 1989). Recent studies of the tectonics of Trinidad and Venezuela incorporate many new data from offshore and onshore petroleum wells and seismic reflection profiles. Algar and Pindell (1993), Babb and Mann (1995), and Flinch et al. (1999) interpreted the Gulf of Paria (Fig. 3) as an extensional pull-apart basin at the right step between two right-lateral strike-slip faults: the El Pilar fault in northern Venezuela and the Central Range (Warm Springs) fault in central Trinidad (Fig. 1b) (also see Sims et al., 1999). Recent geodetic results (Weber et al., 1999, 2000) show that the Central Range fault is curently the active (14 ± mm/y), but aseismic, strike-slip fault in Trinidad. These new data support the pull-apart model and are consistent with Kugler's (1961) interpretation that the southern boundary fault of the Northern Range is a south-dipping normal fault.

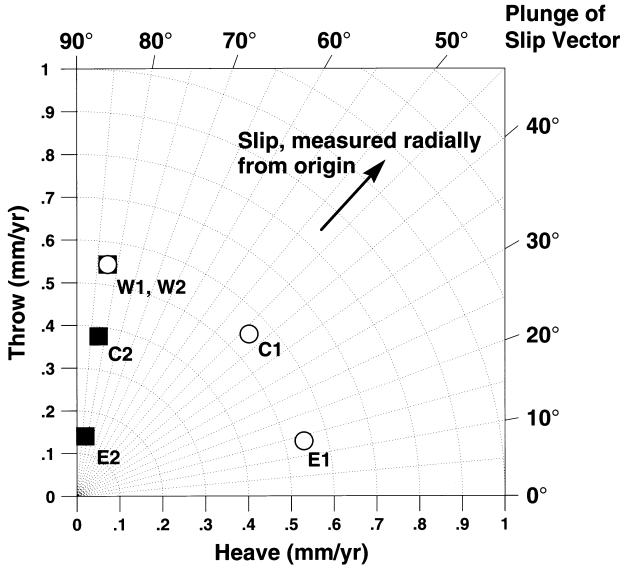

Fig. 11. Graph relating rates of fault slip, fault throw, fault heave, and plunge of slip vector after Ferrill et al. (1996a). W1, C1, E1, and W2, C2, and E2 represent rates of fault slip, fault throw, fault heave, and plunges of slip vectors for western (W), central (C), and eastern (E) Northern Range thermal domains for the first (1) and second (2) fault kinematic models discussed in text. In the first model, lateral changes in rate of throw are explained by a west-to-east decrease in fault dip, but constant rate of dip-slip displacement on the fault. In the second model, lateral changes in rate of throw are explained by changes in rate of dip-slip displacement on a fault with constant dip.

Kinematic data collected from east–west-striking, south-dipping shear bands, and east–west-striking, subvertical, dip-slip faults in thick, cataclastic zones (both of which are pervasive along the southern foot of the Northern Range) also support the range-front normal-fault interpretation (e.g. Figs. 4 and 5). The distribution of deformation temperatures determined in this study is also consistent with this interpretation. The lowest calcite deformation temperatures (150–200°C) come from near the range front (Fig. 9a). There, rocks with type I and type II calcite twins are juxtaposed sharply against 'hotter' Regime 2–3 quartz mylonites (Fig. 9c) across what is most likely a south-dipping normal fault. A group of samples with relatively low-temperature quartz microstructures (Fig. 9c, samples 160-Hilltop, 168-Hilltop, 67-Hilltop, LOP-S-1, and LOP-1) and unreset zircon fission tracks (Fig. 9b, sample MOR) probably mark the position of a similar down-dropped block further west along the range front. The range front fault zone studied in detail at Champs Fleurs (Figs. 1b and 4a) is

probably correlative with Kugler's (1961) Arima fault, and occurs between the Uphill from Hilltop sample (Regime 2) and the 160-Hilltop, 168-Hilltop, and 67-Hilltop samples (Regime 2–1) (Fig. 9c).

We develop two geometric range-front normal-fault models that use laterally changing fault dip and slip rate to explain the east-to-west differential of exhumation and exhumation rate in the Northern Range. These are non-unique forward models. In each, we assume that the east–west-striking, south-dipping (80–85°) shear bands and faults, pervasive along the western range front, mark the orientation of a master normal fault there, rather than that of any other possible related secondary shear surfaces (e.g. R, R', etc.). Neither model disallows an additional component of strike-slip on the range front fault. We simply model only the dip-slip motion, the component of displacement that may have produced the differential exhumation that we observe. The long-term rate of footwall exhumation possible by normal faulting is simply the throw rate component of the total fault slip rate. Throw rate depends on the dip of the fault plane, the rake of the slip vector within the fault plane, and the slip rate (e.g. Fig. 11).

In the first model we assume that the range-front normal fault maintains a constant long-term slip rate of 0.55 mm/y across its entire strike length to match the observed 0.53 mm/y exhumation rate along the proposed 80–85° southward-dipping master fault in the western thermal domain, and allow the dip of this range-bounding fault to vary along strike. Geometrically (Fig. 11), this results in a southward fault dip of 43° in the central domain and of 13° in the eastern domain. The corresponding extensional heave rates along the fault are: 0.08 mm/y (western domain), 0.42 mm/y (central domain), and 0.53 mm/y (eastern domain). Large extensional strains have not been observed along the eastern range front, nor have shallowly dipping, range-bounding faults been found there.

In the next model, we assume that the range-bounding normal fault maintains a constant 80–85° southward dip along its entire strike length, and allow total dip-slip rates to decrease eastward along strike from 0.54 mm/y in the western domain, to 0.38 mm/y in the central domain, and to 0.14 mm/y in the eastern domain, to match our observed exhumation (throw) rates. The corresponding heave rates are (Fig. 11): 0.08 mm/y (western domain), 0.05 mm/y (central domain), and 0.03 mm/y (eastern domain).

Support favoring this second model over the first model may come from the morphology of recent range-front alluvial fans (Fig. 3), although at our present level of understanding of these features this correlation is largely speculative. Nevertheless, in the eastern Northern Range, the range-front alluvial fans are coalesced into a large, laterally extensive bajada. Those along the western range front are small, stubby, individual alluvial fans. This difference may reflect the predominance of vertical sediment aggradation along the western range front, where exhumation and also perhaps uplift rates and basin subsidence, have been the greatest, and that of lateral sediment progradation further east where such rates were lower (e.g. see the analogue study of Ferrill et al., 1996b and references therein).

Although we can match our observed exhumation rates with model rates, it is not realistic to attribute all of the observed Northern Range exhumation to normal faulting. The lack of extremely high overall surface elevations and a systematic east to west increase in elevation across the range implies that erosion must have been vigorous and prevented high footwall topography from developing. Today Trinidad's climate is seasonally wet–dry and tropical, with a mean annual precipitation of 100–150 cm/y (Rand McNally, 1974). In coastal eastern Venezuela, the climate is semiarid tropical, with a mean annual precipitation of 50–100 cm/y; mean annual precipitation decreases further to 25–50 cm/y in coastal central Venezuela (Rand McNally, 1974). This east-to-west decrease in precipitation has a sense opposite to the exhumation rate change that we observe across the Northern Range. This implies that the erosional exhumation contribution was, at best, constant across the Northern Range, and that the range-front (Arima) fault probably played a significant role in differentially exhuming these rocks. Based on the consistent steep dips of shear bands and faults that we observe along the western and central range front, and the morphology of range-front alluvial fans, we favor the second fault kinematic model over the first model.

6.3. Zircon fission-track closure temperature constraints

Our data are consistent with the newly determined higher closure temperature range of 230–330°C for fission track retention in zircon (Tagami et al., 1995; Yamada et al., 1995; Tagami and Shimada, 1996). Calcite microstructure geothermometry data from the northeastern Northern Range indicate peak temperatures of 200–250°C there, and the zircon fission tracks are not reset in these rocks (see Results section above and Fig. 9a, b).

6.4. Absolute microstructural geothermometry at natural strain rates

Several other important insights can be drawn from our study. The experimental results of Hirth and Tullis (1992) used to establish the relative quartz microstructural deformation temperature patterns discussed above could not predict absolute temperature boundaries between microstructural regimes in our naturally deformed rocks. We interpret the quartz microstructures from the northeastern Northern Range as transitional between Regimes 1 and 2 (Fig. 9c), because they generally contain a small proportion of detrital grains with subgrains. Our calcite geothermometry (Fig. 9a) and fission track data (Fig. 9b) from the northeastern Northern Range indicate that these Regime 2 quartz microstructures (Fig. 9c) first appeared at about 200–250°C and at $<$230–330°C. In the northwestern Northern Range, calcite and quartz grains are both completely

dynamically recrystallized (i.e. Regime 3 quartz microstructures are present), and zircon fission track ages are reset. We estimate that the Regime 3 microstructures first appeared there at >230–330°C and <400°C.

In the present study we did not determine the strain rates at which our samples were deformed. It is, however, instructive to consider and discuss some possibilities. The experimentally determined microstructural boundaries of Hirth and Tullis (1992) (Fig. 2) show strong temperature and strain rate dependencies. Typical "background" natural strain rates are estimated to be as low as 10^{-13} to 10^{-15} sec^{-1} (Pfiffner and Ramsay, 1982). Our samples do not come from isolated high-strain or high-strain-rate, structures (e.g. mesoscopic shear zones). We assume "background" natural strain rate values of Pfiffner and Ramsay (1982) and add our new temperature constraints to the graph of Hirth and Tullis (1992) (Fig. 2). The plot suggests that the effect of temperature on quartz microstructural transitions becomes stronger (i.e. the slope of the experimentally determined boundaries flattens) at low (10^{-13} to 10^{-15} sec^{-1}), natural strain rates. (The slope of these boundaries must decrease if the strain rates for our naturally deformed samples were less than 10^{-8} to 10^{-9} sec^{-1}.) The quartz microstructural assemblage transitions mapped in this study may thus serve more generally as geothermometers in other naturally deformed rocks in regions of relatively homogeneous strain rates. Our proposed calibrations, however, need further refining and testing to better constrain the transition temperatures. Also, more attempts should be made to independently estimate natural strain rates.

Calcite microstructures from the carbonate schists in the northwestern Northern Range record the highest calcite deformation temperatures in the range. The calcite in these rocks is completely dynamically recrystallized, giving a lower bound of 300°C for the peak deformation temperatures. A new upper bound of 400°C can be assigned to the complete dynamic recrystallization microstructural assemblage based on the metamorphic mineralogy constraints of Frey et al. (1988).

Acknowledgements

Support for Weber was provided mainly by the Caltech President's Fund and National Science Foundation Grant EAR-9404214. The University of the West Indies Seismic Research Unit, Northwestern University Department of Geological Sciences, The Michigan Space Grant Consortium, and Grand Valley State University supplied some additional support. Part of Ferrill's support was provided by professional development funds from the Nuclear Regulatory Commission, contracts NRC-02-93-005 and NRC-0297-009. This paper does not necessarily reflect the views or regulatory position of the NRC. We thank Christian Teyssier and Martin Burkhard for helpful comments, and Keith Rowley and William Ambeh for logistical assistance.

Appendix A. Fission Track Laboratory Procedures

Apatite and zircon were separated from whole rock samples by standard heavy liquid and magnetic techniques as described in Roden (1991) and Roden and Miller (1991). Apatite and zircon fission track ages were detemined by the external detector method. Small aliquots of 10–20 mg of apatite were mounted in epoxy on glass slides and polished to expose internal grain surfaces. Spontaneous fission tracks in the apatites were revealed by etching for 20 s in 5 M HNO, at 21°C. Aliquots of 10–20 mg of zircon were mounted in teflon and polished to expose an internal surface. Tracks in zircon were etched for 4–20 h in a KOH–NaOH eutectic melt at 225°C. Both apatite and zircon mounts were then covered by a thin sheet of low-uranium muscovite secured by tape.

Samples were irradiated with thermal neutrons to induce fissioning of the ^{235}U in the apatite and zircon at the Oregon State University TRIGA reactor in Corvallis. Fluence standards were two pieces of Coming Glass standards, CN1, apatite, and CN5, zircon, included at the ends of each irradiation package. A thermal neutron fluence of $8 \times 10^{15} n/cm^2$ was obtained for apatite samples and a fluence of 2×10^{15} n/cm^2 was obtained for zircon samples. The Cd ratio (relative to an Au monitor) for this reactor is 14, indicating that the reactor is well-thermalized (Green and Hurford, 1984).

Ages were calculated using a weighted mean zeta calibration factor (Fleischer et al., 1975; Hurford and Green, 1983) for apatite of 103.4 ± 2.3 for standard apatites from the Fish Canyon Tuff, Durango, and Mount Dromedary quartz monzonite and for zircon of 375.6 ± 10.0 for standard zircons from Fish Canyon Tuff and Mount Dromedary quartz monzonite.

The χ^2 (chi-squared) age method of grain age distribution (Brandon, 1992) was used to isolate the youngest group of fission track grain ages that were possibly statistically related. The χ^2 age estimate provides a grouping of the youngest age fraction in a mixture of component grain age populations. In samples in which the zircon or apatite fission track age has been reset, or in which all individual grain ages pass the χ^2 test at the 5% level, the χ^2 age is the same as the pooled fission track age of Green (1981).

References

Aerden, D.G., 1995. Tectonic levels in the Paleozoic basement of the Pyrenees: a review and new interpretation: Discussion. Journal of Structural Geology 17, 1489–1491.

Algar, S.T., 1993. Structural, stratigraphic, and thermo-chronological evolution of Trinidad. Ph.D. thesis, Dartmouth.,College.

Algar, S., Pindell, L, 1993. Structure and deformation history of the Northern Range of Trinidad and adjacent areas. Tectonics 12, 814–829.

Algar, S.T., Heady, E.C., Pindell, J.L., 1998. Fission track dating in Trinidad: Implications for provenance, depositional timing and tectonic uplift. In: Pindell, J.L., Drake, C. (Eds.), Paleogeographic evolution and non-glacial eustasy, northern South America, Society of Economic

Paleontologists and Mineralogists, pp. 111–128. Special Publication 58.

Babb, S., Mann, P., 1995. Style of Late Neogene tectonics of Trinidad revealed through integration of seismic reflection and well data. Geological Society of America Abstracts with Programs 27 (6), 228.

Barr, K.W., 1963. The geology of the Toco District, Trinidad, W. I. Overseas Geological Surveys. Her Majesty's Stationary Office, London.

Brandon, M.T., 1992. Decomposition of fission-track grain-age distributions. American Journal of Science 292, 535–564.

Brandon, M.T., Vance, J.A., 1992. Tectonic evolution of the Cenozoic Olympic subduction complex, Washington state, as deduced from fission track ages for detrital zircons. American Journal of Science 292, 565–636.

Burkhard, M., 1993. Calcite-twins, their geometry, appearance and significance as stress–strain markers and indicators of tectonic regime: a review. Journal of Structural Geology 15, 351–368.

Carreras, J., Capela, I., 1994. Tectonic levels in the Paleozoic basement of the Pyrenees: a review and new interpretation. Journal of Structural Geology 16, 1509–1524.

Carreras, J., Capela, I., 1995. Tectonic levels in the Paleozoic basement of the Pyrenees: a review and new interpretation: Reply. Journal of Structural Geology 17, 1493–1495.

Cobbold, P.R., Cosgrove, J.W., Summers, J.M., 1972. Development of internal structures in deformed anisotropic rocks. Tectonophysics 12 (1), 23–53.

Craig, E.H.C., 1907. Metamorphic rocks of Trinidad. Trinidad and Tobago Government Council Paper 76.

Davis, G.H., 1984. Structural geology of rocks and regions. Wiley and Sons, New York.

Dodson, M.E., 1973. Closure temperature in cooling geochronological and petrological systems. Contributions Mineralogy and Petrology 40, 259–274.

Dodson, M.E., 1979. Theory of cooling ages. In: Jaeger, E., Hunziker, J.C. (Eds.). Lectures in Isotope,Geology, Berlin, Springer-Verlag, p. 329.

Etheridge, M.A., Wilkie, J.C., 1981. An assessment of dynamically recrystallized grain size as a paleopiezometer in quartz-bearing rnylonite zones. Tectonophysics 78, 475–508.

Evans, M.A., Dunne, W.M., 1991. Strain factorization and partitioning in the North Mountain thrust sheet, central Appalachians, USA. Journal of Structural Geology 13, 21–36.

Ferrill, D.A., 1991. Calcite twin widths and intensities as metamorphic indicators in natural low-temperature deformation of limestone. Journal of Structural Geology 13, 667–676.

Ferrill, D.A., Groshong Jr., R.H., 1993. Deformation conditions in the northern Subalpine Chain, France, estimated from deformation modes in coarse-grained limestone. Journal of Structural Geology 15, 955–1006.

Ferrill, D.A., Stirewalt, G.L., Henderson, D.B., Stamatakos, J.A., Morris, A.P., Wernicke, B.R., Spivey, K.H., 1996a. Faulting in the Yucca Mountain Region: Critical Review and Analyses of Tectonic Data from the Central Basin and Range. U.S. Nuclear Regulatory Commission CNWRA 95-017, NUREG/CR-6401.

Ferrill, D.A., Stamatakos, J.A., Jones, S.M., Rahe, B., McKague, H.L., Martin, R.H., Morris, A.P., 1996b. Quaternary slip history of the Bare Mountain Fault (Nevada) from the morphology and distribution of alluvial fan deposits. Geology 24, 559–562.

Ferrill, D.A., 1998. Critical re-evaluation of differential stress estimates from calcite twins in coarse-grained limestone. Tectonophysics 285 (1–2), 77–86.

Fleischer, R.L., Price, P.B., Walker, R.M., 1975. Nuclear Tracks in Solids. Univ. California Press, Berkeley, CA.

Flinch, J, Rambaran, V., Ali, W., De Lisa, V., Hernandez, G., Rodrigues, K., Sams, R., 1999. Structure of the Gulf of Paria pull-apart basin (Eastern Venezuela-Trinidad). In: Mann, P. (Ed.). Caribbean Sedimentary Basins, Elsevier Basins of the World, Elsevier, Amsterdam, pp. 477–494.

Foland, K.A., Speed, R., Weber, L, 1992a. Geochronologic studies of the hinterland of the Caribbean orogen of Venezuela and Trinidad. Geological Society of America Abstracts with Programs 24, 148.

Foland, K.A., Speed, R.C., 1992b. Geochronology of metamorphic rocks of the Northern Range. Symposium on regional structure and tectonic evolution of northern Trinidad and vicinity, Programme and Abstracts, Geological Society of Trinidad and Tobago, 11.

Frey, M., 1987. Metamorphism of clastic sedimentary rocks. In: Frey, M. (Ed.). Low temperature metamorphism, Blackie and Son Ltd, London, pp. 9–57.

Frey, M., Saunders, L, Schwander, H., 1988. The mineralogy and metamorphic geology of low-grade metasediments, Northern Range, Trinidad. Journal of the Geological Society of London 145, 563–575.

Garcia-Sansegundo, L., 1996. Hercynian structure of the Axial Zone of the Pyrenees: the Aran Valley cross-section (Spain–France). Journal of Structural Geology 18, 1315–1325.

Gleadow, A.J.W., Duddy, I.R., 1981. A long-term annealing experiment for apatite. Nuclear Tracks and Radiation Measurements 5, 169–174.

Green, P.F., 1981. On the cause of the shortening of spontaneous fission tracks in certain minerals. Nuclear Tracks 4 (2), 91–100.

Green, P.F., 1988. The relationship between track shortening and fission-track retention in apatite: combined influences of inherent instability, annealing anisotropy, and length bias and system calibration. Earth and Planetary Science Letters 89, 335–352.

Green, P.F., Hurford, A.J., 1984. Thermal neutron dosimetry for fission track dating. Nuclear Tracks and Radiation Measurements 9, 231–241.

Griggs, D.T., Blacic, J.D., 1965. Quartz: Anomalous weakness of synthetic crystals. Science 147, 292–295.

Groshong, R.H., Pfiffner, O.A., Pringle, L.R., 1984. Strain partitioning in the Helvetic thrust belt of eastern Switzerland from the leading edge to the internal zone. Journal of Structural Geology 3, 5–18.

Harris, A.G., 1979. Conodont color alteration, an organo-mineral metamorphic index, and its application to Appalachian basin geology. In: Scholle, P.A., Schluger, P.R. (Eds.). Aspects of diagenesis. Society of Economic Paleontologists and Mineralogists Special Publication 26, , pp. 3–16.

Harrison, T.M., McDougall, I., 1980. Investigations of an intrusive contact, northwest Nelson, New Zealand-1: Thermal, chronological and isotropic constraints. Geochimica et Cosmochimica Acta 44, 1985–2003.

Hirth, G., Tullis, J, 1992. Dislocation creep regimes in quartz aggregates. Journal of Structural Geology 14, 145–159.

Hobbs, B.E., Means, D.W., Williams, P.F., 1976. An outline of structural geology. Academic Press, New York.

Hurford, A.J., Green, P.F., 1983. The zeta age calibration of fission track dating. Isotope Geoscience 1, 285–317.

Kish, H., 1987. Correlation between indicators of very low-grade metamorphism. In: Frey, M. (Ed.). Low temperature metamorphism, Blackie and Son Ltd, London, pp. 227–299.

Kugler, H.G., 1961. Geological map and sections of Trinidad. Orell, Zurich (Also in: Treatise on the Geology of Trinidad, compiler, Kugler, H.G., Part 2 or part of Part 3. Natural History Museum, Basel, Switzerland), scale 1:100,000.

Law, R.D., 1990. Crystallographic fabrics: a selective review of their applications to research in structural geology. In: Knipe, R.L., Rutter, E.H. (Eds.). Deformation mechanisms, rheology and tectonics., Geological Society, pp. 335–352 Special Publication 54.

Liou, J.G., Maruyama, S., Cho, M., 1987. Very low-grade metamorphism of volcanic and volcaniclastic rocks-mineral assemblages and mineral facies. In: Frey, M. (Ed.). Low temperature metamorphism, Blackie and Son Ltd, London, pp. 59–113.

Mancktelow, N.S., Grasemann, B., 1997. Time-dependent effects of heat advection and topography on cooling histories during erosion. Tectonophysics 270 (314), 167–195.

Milliman, J.D., Syvitski, P.M., 1992. Geomorphic/Tectonic control of sediment discharge to the ocean: the importance of small mountain rivers. Journal of Geology 100, 525–544.

Naeser, C.W., Faul, H., 1969. Fission-track annealing in apatite and sphene. Journal of Geophysical Research 754, 705–710.

Naeser, C.W., 1981. The fading of fission-tracks in the geologic environment-data from deep drill holes. Nuclear Tracks and Radiation Measurements 5, 248–250.

Passchier, C.W., Trouw, R.A.J., 1996. Microtectonics. Springer-Verlag, Berlin.

Pindell, J.L., 1985. Alleghenian reconstruction and subsequent evolution of the Gulf of Mexico, Bahamas, and Proto-Caribbean. Tectonics 4, 1–39.

Pfiffner, O.A., Ramsay, J.G., 1982. Constraints on geological strain rates: arguments from finite strain states of naturally deformed rocks. Journal of Geophysical Research 87 (B1), 311–321.

Potter, H.C., 1973. The overturned anticline of the Northern Range near Port of Spain. Journal of the Geological Society of London 129, 133–138.

Rand McNally, 1974. The new international atlas. Rand McNally and Co., Chicago.

Robertson, P., Burke, K., 1989. Evolution of the southern Caribbean plate boundary, vicinity of Trinidad and Tobago. American Association of Petroleum Geologists Bulletin 73, 490–509.

Roden, M.K., 1991. Apatite fission-track thermochronology of the southern Appalachian Basin: Maryland, West Virginia, and Virginia. Journal of Geology 99, 41–53.

Roden, M.K., Miller, D.S., 1991. Tectono-thermal history of Hartford, Deerfield, Newark and Taylorsville Basins, eastern United States, using fission-track analysis. Swiss Bulletin of Mineralogy and Petrology 71, 187–203.

Russo, R.M., Speed, R.C., 1992. Oblique collision and teconic wedging of the South American continent and Caribbean terranes. Geology 20, 447–450.

Saunders, J.B., 1972. Recent paleontological results from the Northern Range of Trinidad. Transactions of the Fourth Latin American Geological Conference, Trinidad and Tobago, pp. 781–796.

Schmidt, S.T., Robinson, D., 1997. Metamorphic grade and porosity and permeability controls on mafic phyllosilicate distributions in a regional zeolite to greenschist facies transition of the North Shore Volcanic Group, Minnesota. Geological Society of America Bulletin 109, 683–697.

Sims, D., Ferrill, D.A., Stamatakos, J.A., 1999. Role of a ductile decollement in the development of pull-apart basins: Experimental results and natural examples. Journal of Structural Geology 21, 533–554.

Spears, F.S., 1993. Metamorphic phase equilibria and pressure-temperature-time paths, Mineralogical Society of America Monograph.

Speed, R.C., 1985. Cenozoic collision of the Lesser Antilles arc and continental South America and the origin of the El Pilar fault. Tectonics 4, 41–69.

Speed, R.C., 1986. Cenozoic tectonics of the southeastern Caribbean and Trinidad. In: Rodrigus, K. (Ed.). Transactions of the First Geological Conference of Trinidad and Tobago, General Printers, San Juan, Trinidad, pp. 270–280.

Summerflield, M.A., Hulton, N.L., 1994. Natural controls of fluvial denudation rates in major world drainage basins. Journal of Geophysical Research 99 (B7), 13871–13883.

Sutter, H., 1960. The General and Economic Geology of Trinidad, W. I. Overseas Geological Surveys. Her Majesty's Stationary Office, London.

Tagami, T., Ito, H., Nishimura, S., 1990. Thermal annealing characteristics of spontaneous fission tracks in zircon, Chemical Geology. Isotope Geology Section 80, 159–169.

Tagami, T., Carter, A., and Hurford, A.J., 1995. Natural long-term annealing of zircon fission-track system in Vienna Basin deep boreholes: Constraints upon the closure temperature and partial annealing zone, Chemical Geology, Isotope Geology Section 130(1–2), 147–157.

Tagami, T., Shimada, C., 1996. Natural long-term annealing of the zircon fission track system around a granitic pluton. Journal of Geophysical Research 101, 8245–8255.

Teichmuller, M., 1987. Organic material and very low-grade metamorphism. In: Frey, M. (Ed.). Low temperature metamorphism, Blackie and Son Ltd, London, pp. 114–160.

Turner, F.J., Weiss, L.E., 1963. Structural analysis of metamorphic tectonites. McGraw-Hill, New York.

Turner, F.J., Orozco, M., 1976. Crystal bending in metamorphic calcite and its relations to associated twinning. Contributions to Mineralogy and Petrology 57, 8397.

Wadge, G., Macdonald, R., 1985. Cretaceous tholeites of the northern continental margin of South America: the Sans Souci Formation of Trinidad. Journal of the Geological Society of London 142, 297–308.

Wagner, G.A., 1968. Fission-track dating of apatites. Earth and Planetary Science Letters 4, 41–415.

Wagner, G.A., Van den Haute, R, 1992. Fission track dating. Kluwer Academic Publishers, Dordrecht.

Weber, J.L., Saleh, L., Balkaransingh, S., Ambeh, W., Dixon, T., and Webb, F., 1999. 1901-1995 Geodetic displacernents in Trinidad: new constraints on local earthquake hazards and Caribbean-South American neotectonics, American Geophysical Union Transactions, EOS 80, 46, p.276.

Weber, J., Dixon, T., DeMets, C., Ambeh, W., Jansma, P., Mattiol, G., Salah, J., Sella, G., Bilham, R., Pérez, O., 2000. A GPS estimate of relative motion between the Caribbean and South American plates, and geologic implications for Trinidad and Venezuela. Geology (in press).

Yamada, R., Tagami, T., Nishimura, S., Ito, H., 1995. Annealing kinetics of fission tracks in zircon: an experimental study, Chemical Geology. Isotope Geology Section 122, 249–258.

Zaun, P.E., Wagner, G.A., 1985. Fission track stability in zircons under geological conditions. Nuclear Tracks and Radiation Measurements 10, 303–307.